

MODELING INTERANNUAL AND DECADAL VARIABILITY IN THE HUMBOLDT CURRENT UPWELLING SYSTEM

Vincent Combes ⁽¹⁾, Emanuele Di Lorenzo ⁽¹⁾, Fabián Gómez ⁽²⁾,
Samuel Hormazabal ⁽²⁾, Ted P. Strub ⁽³⁾ and Dian Putrasahan ⁽⁴⁾

⁽¹⁾ *School of Earth and Atmospheric Sciences, Georgia Institute of Technology
Atlanta, Georgia, USA*

⁽²⁾ *Departamento de Geofísica, Universidad de Concepción, Chile*

⁽³⁾ *College of Oceanic and Atmospheric Sciences, Oregon State University,
Corvallis, Oregon, USA*

⁽⁴⁾ *Scripps Institution of Oceanography, La Jolla, California, USA*

In preparation for *Journal of Physical Oceanography*
July 23, 2009

Corresponding author:

Vincent Combes
School of Earth and Atmospheric Sciences
Georgia Institute of Technology
311 Ferst Drive, Atlanta, GA, 30332-0340
voice: 404-894-1749, fax: 404-894-5638
email: Vincent.Combes@eas.gatech.edu

Abstract

The Humboldt Current System (HCS) is the one of the world's most productive regions in fish landings, providing ~20% of the world marine catches despite covering less than 1% of the world's ocean surface. This high productivity results principally from the upwelling of nutrient-rich water in the photic zone. This study investigates the HCS variability using a free-surface, hydrostatic, eddy resolving primitive equation model combined with a passive tracer advection-diffusion equation. The upwelling variability, important in understanding the ecosystem dynamics, is examined using a model passive tracer, continuously released at the coast in the subsurface between 150 and 250 m depth. The concentration of that tracer observed at the surface can therefore be considered as an index of coastal upwelling. Different model experiments are conducted to explore the sensitivity of the HCS upwelling to different air-sea fluxes of momentum and atmospheric and oceanic teleconnections to ENSO. On average, we find that the model runs forced by ECMWF and QSCAT wind stress compare better with observations than the experiment forced by NCEP wind stress, with strong upwelling off Peru (5°S - 16°S) and central Chile (27°S - 34°S) and significantly weaker upwelling in the North Chile Region (18°S - 24°S), consistent with the strength of coastal upwelling-favorable winds. Temporal variability is nevertheless well reproduced by NCEP, when comparing model and in situ coastal sea surface height data. There is evidence, in this region, that both changes in surface wind and coastally trapped Kelvin waves control the variability of the coastal upwelling. The effect of ocean remote forcing is assessed by comparing the output of two model simulations which does and does not include the presence of waves at their boundaries. The passive tracer

approach indicates that, off the coast of Peru, the El Niño Southern Oscillation (ENSO) strongly modulates the strength of coastal upwelling principally due to the propagation of downwelling equatorial Kelvin waves (particularly strong during El Niño years) rather than changes in local wind stress. Our results indicate that the central Chile region is also very sensitive to Kelvin waves generated at the equator, considerably reducing the upwelling during strong El Niño events, therefore impacting the ecosystem variability. There is also a decadal variability signal that seems to respond to the second mode of sea level pressure in this region.

1. Introduction

The eastern boundary system of the Southeast Pacific, referred to as the Humboldt Current System (HCS; named after the Prussian explorer Alexander von Humboldt), calls for special consideration due to its high biological productivity and ecosystem efficiency. The HCS supports approximately 18-20% of the fish catches worldwide (http://www.eoearth.org/article/Humboldt_Current_large_marine_ecosystem), for the most part constituted of anchovies, sardines and jack mackerel (Arcos et al., 2001; Alheit and Niquen, 2004). This high productivity region is driven by the upwelling of cold, nutrient-rich water brought to the surface. Strub et al. (1998) divide the coastal upwelling system into three different regions according to their disparities in mean and seasonal cycle. First, an area of year-round upwelling off Peru, which is stronger in austral winter; secondly, a region of weaker upwelling off northern Chile, which tends to be stronger in spring and summer; and finally a seasonally strong upwelling system off central Chile in spring and summer, with downwelling in fall and winter.

On interannual time scales, the El Niño Southern Oscillation (ENSO) is the leading mode of variability of the HCS. Previous studies (Hormazabal et al., 2002) suggest that poleward propagating coastally trapped Kelvin waves are generated at the equator and play an important role in the upwelling variability. These waves are especially strong during E. Niño events. Shaffer et al., (1997) speculate on the possible effects of remote ocean forcing on the marine living resources. Indeed, since coastal-trapped waves strongly modify coastal upwelling, such waves have a significant influence on the pelagic ecosystem. For example, during the waves' downwelling phase, the deepening of the

thermocline tends to make the upper layer warmer and deprived of nutrients, reducing biological productivity.

This study focuses on interannual and decadal upwelling variability and uses a model passive tracer to represent the coastal subsurface waters. The passive tracer is here used as a proxy for coastal upwelling strength and for transport of nutrient-rich coastal waters. The present approach aims to characterize the coastal upwelling statistics. Another objective of this study is to better quantify the influence of the equatorial Kelvin waves and to determine if that influence is stronger during El Niño events.

This paper is organized as follows. The following section describes the model experiments and the tracer approach used in this study. Section 3 discusses the mean circulation of the HCS and the interannual upwelling variability. Section 3 will also try to estimate the effects of remote ocean forcing on the upwelling variability. Section 4 provides a summary of the results.

2. Model and Tracer experiment setup

2.a. Domain and model experiments

The Regional Ocean Modeling System (ROMS; Shchepetkin and McWilliams, 2005) is a three dimensional, free-surface, hydrostatic, eddy-resolving primitive equation ocean model. The model employs orthogonal curvilinear coordinates in the horizontal and terrain-following coordinates in the vertical with higher resolution at the surface. ROMS has already been used successfully to simulate eastern boundary current systems (*California System*: Di Lorenzo et al., 2005; Marchesiello et al., 2003; *Benguela System*: Penven et al., 2001; *Peru System*: Penven et al., 2005).

The grid extends southward from 2°S to 43°S and westward from the west coast of South America to 92°W. Based on the spatial pattern of the mean upwelling We refer to the Peruvian coast as the region between 5°S-18°S, the northern Chilean coast as the region between 18°S-27°S, and the central Chilean coast as the region between 27°S and 40°S. The grid has an average horizontal resolution of 20 km with 30 levels in the vertical and a minimum depth for the model bathymetry of 15m. The resolution is found to be sufficient for capturing mesoscale eddy features.

We conduct different model experiments to explore the sensitivity of the HCS upwelling to different air-sea fluxes of momentum and to its remote connection to ENSO, both atmospheric and oceanic (Table 1). The model was first spun up for 56 years (EXP_SPIN) with monthly-mean surface forcing from the National Center for Environmental Prediction/National Center for Atmospheric Research reanalysis (NCEP/NCAR; Kalnay et al. 1996) and initial and boundary conditions from a high-resolution MOM3-based Ocean General Circulation Model (OGCM) code optimized for the Earth Simulator (OFES; Masumoto et al., 2004). The OFES simulation uses a nearly-global domain which extends from 75°S to 75°N, with a horizontal resolution of 0.1° and 54 vertical levels, forced by daily-mean surface wind stress, heat, and freshwater fluxes derived from the NCEP/NCAR reanalysis. For the experiments named EXP_NCEP, EXP_QSCAT, EXP_ECMWF, EXP_NCEP_BRY (Table 1), the freshwater surface fluxes are set to a corrected monthly climatology derived from EXP_SPIN in which the surface salinity is nudged to the observed climatology and the resulting flux correction is saved. EXP_QSCAT, EXP_ECMWF and EXP_NCEP use the final state of EXP_SPIN as initial

condition and the output of the OFES experiment as lateral open ocean boundary condition. EXP_QSCAT and EXP_ECMWF differ from EXP_NCEP in their surface momentum fluxes, which are prescribed to wind stress derived respectively from SeaWINDS onboard the NASA's QuikSCAT satellite (QSCAT) and from the European Centre for Medium-Range Weather Forecasts (ECMWF; Uppala et al., 2005). Finally EXP_NCEP_BRY differs from EXP_NCEP in the boundary condition. While EXP_NCEP uses a time-dependent open ocean boundary condition, EXP_NCEP_BRY uses a climatology state which does not include the presence of equatorial Kelvin waves, important during El Niño years.

2.b. Tracer experiment setup

The Humboldt Current System (HCS) is a highly productive region, resulting from strong coastal upwelling (Strub et al., 1998). The upwelling variability, critical to the understanding of the ecosystem dynamics, is characterized using a passive tracer advection-diffusion equation with a decay term as in Combes et al., 2009:

$$\frac{\partial P}{\partial t} + \underline{u} \cdot \nabla P = A_H \nabla_H^2 P + \frac{\partial}{\partial z} \left(A_V \frac{\partial P}{\partial z} \right) - \frac{P}{\tau} + Q(x, y, z)$$

where P is the passive tracer concentration, $A_H = 5 \text{ m}^2\text{s}^{-1}$ is the horizontal diffusivity, A_V the vertical diffusivity obtained by a KPP scheme (Large et al, 1994), Q a time independent source term and τ is the decay timescale. The source term is such that the passive tracer is set to 1 over a region from the coast to 50 km offshore and in the subsurface from 150m to 250m depth. These depths were chosen to mimic the distribution of nutrient-rich water that is brought to the surface during normal upwelling, while remaining below the

pycnocline when the pycnocline deepens during El Nino events and the passage of coastally trapped waves. We will consider the concentration of tracer found at the surface as a measure of coastal upwelling and refer to it using the term “upwelling”. We ask the reader to remember that the terms “upwelling” and “downwelling” indicate the net response in the ocean, rather than the forcing by winds and CTW’s. Finally, to avoid an infinite growth of passive tracer, the advection-diffusion equation also includes a decay timescale τ set to 1 year, sufficient to track the path of the subsurface passive tracer in the model domain.

We first test if the passive tracer approach reproduces the upwelling circulation in a realistic way. Figure 1 shows a snapshot from EXP_ECMWF for the month January 1999 of the modelled sea surface height (SSH; Fig 1a), surface passive tracer (Fig 1b), and the vertical profiles of temperature (Fig. 1d) and passive tracer (Fig. 1e) across the black transect on Fig 1b. The injection of passive tracer at the coast in the subsurface between 150 and 250m depth, described in the previous paragraph, is illustrated on Fig 1e, which shows the vertical advection of tracer on the coastal boundary followed by a surface offshore advection. The coastal upwelling is also pictured on Fig. 1d as a longitudinal gradient in the temperature field with colder temperature along the coast. Fig. 1b exhibits two strong upwelling regions off Peru and off central Chile for January 1999, associated with a high concentration of passive tracer along the coast, which then is advected offshore by surface currents. Those two highly productive regions are also observed in the coastal chlorophyll-a distribution (measured by SeaWiFS satellite; Fig. 1c). South of 40°S, we notice low passive tracer concentrations (grey oval in Fig 1b) compared to the Chlorophyll-a (Fig 1c). The lack of passive tracer is associated with

predominant downwelling-favorable winds (second grey oval on Fig 1b). The source of higher Chl-a concentration needs further investigation and may be linked to the high river runoff in this region, among others the Bio-Bio river ($\sim 37^\circ\text{S}$) and the Valdivia river ($\sim 40^\circ\text{S}$). In addition to the advection by surface currents (Fig 1b), offshore transport of nutrient-rich coastal water, simulated by the passive tracer experiment, also occurs in the subsurface. Indeed the westward transport associated with modelled cyclonic eddies for January 1999 is evident in the vertical sections of tracer concentration and temperature (grey boxes in Fig. 1d-e). These cyclonic eddies, characterized by a negative SSH anomaly (Fig. 1a), are associated with a colder core than the surrounding water (Fig. 1d). The presence of tracer concentration in the eddy cores (Fig. 1e) suggests that the cold anomaly found in the eddy interior is advected from the coastal region, which also implies a cross-shore mixing of other important biochemical quantities (Correa-Ramirez et al., 2007).

3. Results

3.a. Mean Circulation of the Humboldt Current System (HCS)

Previous modelling and observational studies (Strub et al., 1998) depict the HCS, also known as the Peru-Chile current system (PCCS), as an interaction of three major and permanent ocean currents. At approximately 43°S , a broad eastward current (West Wind Drift, WWD) diverges into the poleward Cape Horn Current (CHC, south of our model domain) and the equatorward Peru Current (PC). Specific to eastern boundary current systems, a permanent poleward flow also develops in the subsurface off the coast of Peru and Chile, known as the Peru-Chile UnderCurrent (PCUC). It is identified by its water mass characteristics (Gunther, 1936): saltier, richer in nutrients and lower in

oxygen than the surrounding water. The principal atmospheric systems that influence those surface currents are the Intertropical Convergence Zone (ITCZ) close to the equator, the South Pacific High in the midlatitudes and polar front storms in the high latitudes (Strub et al., 1998).

The mean of the meridional component of the surface wind stress is shown in Fig. 2a for the period after 1999 when all datasets overlap. The QSCAT satellite observation mean meridional wind stress shows three distinct regions at the coast, with local maxima of upwelling-favorable winds off Peru (around 14°S) and central Chile (around 30°S) and a region of weak positive (equatorward) meridional wind off northern Chile. In Fig. 2a, we also can notice, in particular off Chile, that the ECMWF meridional winds have a narrow decrease next to the coast that is not apparent in QSCAT. Nevertheless, an additional experiment (not analyze in this study) used “corrected” ECMWF coastal winds, formed by interpolating the offshore wind to the coast. Results from this experiment show that the narrow coastal decrease in ECMWF wind speeds does not produce any effect in the advection of tracer or SSH.

While the spatial pattern of the ECMWF wind reanalysis is consistent (albeit slightly overestimated in magnitude) with that from QSCAT, important differences appear with the NCEP mean meridional wind stress at the coast. Those differences in the air-sea fluxes of momentum between NCEP and QSCAT are reflected in the coastal SSH (Figure 2b), which shows a rise in SSH next to the coast for NCEP forcing. For both ECMWF and QSCAT, the mean SSH response in Figure 2b shows a band of negative anomalies along the coast and at the southern boundary, which generates equatorward PC and the eastward WWD at the surface. These fields are more consistent with satellite observations

(derived from AVISO satellite maps available at <http://www.jason.oceanobs.com>) and surface drifters (Niiler et al., 2003). The AVISO SSH field exhibits a deeper SSH low at the coast and stronger zonal gradients than the model, but the spatial SSH pattern is preserved in the model runs. This minimum in SSH is incorrectly located offshore in EXP_NCEP, consistent with the curl of the NCEP surface wind stress. Even though the mean SSH from EXP_NCEP has major coastal differences with observations, we will see later that its temporal variability is highly correlated with in-situ data.

By using the presence of passive tracer at the surface to indicate upwelling, experiments EXP_QSCAT and EXP_ECMWF suggest that those atmospheric conditions produce a mean strong upwelling off Peru, persistent but weaker upwelling off northern Chile, and strong upwelling off central Chile (Fig 2d). Fig 2d also shows the direct relation between the mean alongshore wind stress component (upwelling-favorable winds) and the concentration of tracer found at the surface. The slightly overestimated ECMWF coastal wind stress can also be observed in the surface passive tracer with slightly stronger upwelling regions, compared to EXP_QSCAT. On the other hand, the weak coastal NCEP wind stress (Fig. 2a or black vectors on Fig. 2c) does not allow those two strong permanent upwelling regions to develop off Peru and central Chile (white boxes in Fig 2c).

The same upwelling cells can also be observed in the mean Sea Surface Temperature (SST) fields (Fig. 2c). Both EXP_ECMWF and EXP_QSCAT show bands of cold water off the coasts of Peru (somewhat wider in EXP_ECMWF reflecting the narrow wind gap off Peru) and central Chile, also apparent in satellite image SST (derived from the blended AVHRR-AMSR SST satellite

maps available at <ftp://eclipse.ncdc.noaa.gov/pub/OI-daily-v2/NetCDF-uncompress/>). In contrast, EXP_NCEP again does not capture those regions of upwelled cold water because of weaker NCEP coastal wind forcing (white boxes in Fig 2c).

3.b. Interannual Variability of the Peru and Central Chile upwelling systems

To explore the interannual upwelling variability in the Humboldt Current System, we examine the time series of SSH anomalies (SSHa) and tracer concentration anomalies, where the anomalies are defined by removing the monthly mean seasonal cycles. Fig 3 shows a comparison of the model coastal sea level height anomalies (red lines) with in situ records (blue lines; provided by The University of Hawaii Sea Level Center available at <http://ilikai.soest.hawaii.edu/uhslc/data.html>) at five different locations along the coast off Peru and Chile; (Lobos de Afuera ($6^{\circ}56'S$), Callao ($12^{\circ}03'S$), Arica ($18^{\circ}28'S$), Antofagasta ($23^{\circ}39'S$) and Valparaiso ($33^{\circ}02'S$)). While Fig 2 shows the poor representation of the mean spatial pattern of SSH in EXP_NCEP, Fig 3 indicates that both EXP_ECMWF and (in particular) EXP_NCEP model hindcasts are nevertheless able to explain a significant fraction of the in situ sea level variance, especially off Peru. For example, the model SSHa captures the major positive ENSO events (1982; 1998), represented by a positive peak in the SSHa, characteristic of an anomalous downwelling condition. Off central Chile, both in-situ and model SSHa also exhibit a decadal frequency superimposed on the ENSO cycle.

Confident that the model adequately reproduces interannual variability in upwelling for EXP_ECMWF and EXP_NCEP, we perform an empirical

orthogonal function (EOF) analysis of the passive tracer concentration anomaly off Peru and central Chile (Fig. 4). Off Peru, the leading EOF (Fig 4a,e) explains more than 50% of the variance and shows a similar spatial pattern between the output of EXP_NCEP (Fig 4a) and EXP_ECMWF (Fig 4e) with negative values off the coast. The temporal modulations of these patterns, which are represented by the principal component time series (PC 1; Fig 4b,f), reflect the variability of the strength of anomalous coastal upwelling (negative values of PC 1) and downwelling (positive values of PC 1). Both EXP_NCEP and EXP_ECMWF shows that the first mode of variability of the passive tracer (PC 1; Fig 4b,f) is significantly correlated with the Niño 3.4 index (purple lines; $R=0.37$ for EXP_NCEP, $R=0.44$ for EXP_ECMWF) with downwelling conditions during positive ENSO events (positive index).

Off central Chile, the first mode of upwelling variability for EXP_NCEP (Fig. 4d) shows the superposition of a high frequency signal, correlated with the Niño 3.4 index and a signal of multi-decadal variability, which is also evident in the in-situ SSHa data shown on the most southern tidal gauge presented on Fig 3. For EXP_ECMWF, those two signals are split into the first and second EOF. Indeed, while the first PC (Fig 4h) shows the multi-decadal variations, the second PC (Fig 4j) displays a mode correlated with the ENSO ($R=0.28$), which is spatially consistent with the one captured by EXP_NCEP as mode 1. It is also instructive to notice that the separation of these two time scales in EXP_ECMWF surface tracers off Chile (Figs 4h – 4j) also separates the spatial patterns. In Figure 4g, the multi-decadal signal includes the north-south gradient, with higher upwelled tracer depicted in a band running from South-East to North-West off Punta Lavapie near 38°S . The ENSO signal in Figure 4i

represents the onshore-offshore gradient of tracer, especially between 28°S-32°S.

We explore the source of the multi-decadal signal by characterizing the local atmospheric forcing using an EOF decomposition of the sea level pressure anomalies (SLPa) from NCEP/NCAR reanalysis, since NCEP/NCAR provides the consistent forcing of OFES and the regional model. The first SLPa EOF (Fig 4o and 4p) explains 83% of the atmospheric variability and closely tracks the Antarctic Oscillation index (also referred to as the Southern Annular Mode, purple line on Fig 4p). In contrast, the second EOF and PC (Figs 4q and 4r) exhibits the multi-decadal variations found in the tracer concentration of PC1 EXP_NCEP (green line on Fig. 4r and 4d) and EXP_ECMWF (blue line on Fig. 4r and 4h). The regression of the surface NCEP wind stress onto the PC2 time series of SLPa (the black vectors on Fig 4q) shows a stronger upwelling-favorable component off the cape, around 38°S, which coincides with the region of high tracer concentration in the EOF1 of EXP_ECMWF (Fig. 4g; which is the cleanest separate component identified as multi-decadal). This also suggests that the oceanic multi-decadal signal in the upwelling system is directly forced by the local atmospheric variability. To complete the comparison between the second EOF of SLP and the first EOF of tracer concentration off central Chile for EXP_NCEP and EXP_ECMWF, Fig 4r indicates the correlation between their PCs. As expected, the correlation between PC2 of SLP and PC1 of tracer from EXP_NCEP (red and green lines on Fig4r; $R=0.33$) is lower than the correlation with the tracer concentration from EXP_ECMWF (red and blue lines on Fig4r; $R=0.45$), since the PC1 from EXP_NCEP (Fig 4d) includes both the multi-decadal signal and the ENSO signal. For information, Fig 4o also shows the

regression of the surface NCEP wind stress onto the PC1 time series of SLPA (which correlates with the AAO index) and exhibits a similar pattern to that in fig 4q but with a weaker meridional component.

3.c. Effects of remote oceanic forcing

The previous section illustrated, using a passive tracer approach, that much of the interannual upwelling variability off Peru and central Chile is caused by the ENSO cycle. ENSO impacts the circulation through local changes in surface wind stress (Halpern, 2002) and via coastally trapped Kelvin waves (Pizarro et al., 2002). Off Peru, the deepening of the thermocline is mostly related to coastal trapped waves of equatorial origin (Hill et al., 1998), with actually little strengthening of equatorward winds (Halpern, 2002). Spillane et al. (1987) also supports this hypothesis by looking at the sea level variability and shows that intraseasonal variability (~50-days fluctuations) off the South American coast is linked primarily to poleward coastally trapped Kelvin waves forced by eastward wind events in the western and central Pacific, more prominent during the onset of El Niño events.

Using the model experiments we now separate the effects of remote oceanic forcing (waves generated at the equator) from local changes in the air-sea momentum flux on the interannual upwelling variability. To do so, we perform two experiments with the same surface forcing and initial condition, one using time-dependent ocean boundary conditions (EXP_NCEP, used in the previous analysis) and the other with prescribed climatological boundary conditions (EXP_NCEP_BRY; see Table 1). In other words, while EXP_NCEP possesses poleward-driven coastally trapped Kelvin wave pulses in its northern ocean boundary, EXP_NCEP_BRY filters the wave signals from the boundaries

by prescribing monthly climatological values at the oceanic open boundaries. Since the previous section shows that the interannual variability of SSH from EXP_NCEP shows a good agreement with coastal in-situ measurements, we decide to continue with NCEP surface forcing to be consistent with the OFES run forced by NCEP winds which provides the boundary condition for each of our simulations. Fig 5a shows the difference in tracer concentration at the surface between EXP_NCEP and EXP_NCEP_BRY during the strong 1997-1998 El Niño event. During this time, strong downwelling eastward Kelvin waves are generated at the equator (Hormazabal et al., 2002) and enter the model domain as poleward coastal trapped Kelvin waves. The non-zero values at the coast in Fig 5a show the importance of those waves in the upwelling variability off the west coast of South America. The negative values at the coast indicate stronger upwelling when the simulation does not include the downwelling equatorial waves from the northern boundary (EXP_NCEP_BRY), using the same wind forcing. Two regions show a strong response to the propagation of equatorial downwelling waves during the 1997-1998 El Niño year (EXP_NCEP): off the coast of Peru and also south of 30°S off central Chile. Off Chile, Fig 5b compares the time series of the surface tracer concentration anomaly for EXP_NCEP (blue line) and for EXP_NCEP_BRY (black line) with the surface meridional wind stress from the NCEP/NCAR reanalysis (NCEP_Svstr; green line), for the period 1980-2007 when two major El Niño events occurred (1982 and 1998). The non-perfect correlation ($R=0.67$) between EXP_NCEP (blue) and EXP_NCEP_BRY (black) supports the previous idea that the choice of boundary condition is important in reproducing the upwelling circulation.

The importance of the poleward propagation of coastally trapped Kelvin waves can also be seen when comparing those two time series to the anomalous meridional wind stress. Fig. 5b focuses on the southern region. Indeed, off central Chile, while the surface meridional wind stress explains $R^2=39.7\%$ of the upwelling variance in EXP_NCEP_BRY (black line), it only explains $R^2=22.1\%$ of the upwelling variance in EXP_NCEP (blue line). The major differences arise during the strong El Niño years (gray circles; 1982 and 1998). For example, during the years 1982-83, the surface tracer concentration in EXP_NCEP_BRY (black line) increases as a direct response to an increase (ie upwelling-favorable) of the surface wind stress (dash green line). At the same time, EXP_NCEP (blue line) shows a more downwelling condition, reflecting the presence of the strong downwelling coastally trapped Kelvin propagating poleward during the El Niño event. Similar dynamic relationships can be seen during the 1998 El Niño event.

To assess the degree of importance of those waves in explaining the coastal upwelling variability, we compute the correlation of the tracer concentration time series between EXP_NCEP and EXP_NCEP_BRY (Fig 5c). Fig. 5c indicates that the equatorial trapped Kelvin waves explain more upwelling variability at lower latitude along the coast, decreasing the correlation coefficient from around 0.7 off Central Chile to an almost zero correlation off Peru. However, even though the correlation off central Chile is as high as 0.7, the temporal upwelling variability is strongly affected by the presence of those waves during strong El Niño events, as seen in the previous paragraph (Fig 5b). The maps of correlations between the two experiments for the tracer concentrations (Fig 5c) and for the SSH fields (Fig 5d) show similar

patterns along the coast. Fig 5d gives some indication also of the offshore effects. In particular, the region of high Eddy Kinetic Energy (EKE, white contours on Fig 5d) off the coast of Chile around 30°S displays an almost zero correlation between the SSH time series of the two experiments, EXP_NCEP and EXP_NCEP_BRY. This suggests that the intrinsic ocean variability that creates the high values of EKE in this region is strongly affected by CTW's originating at the northern boundary.

To further clarify the upwelling variability due to remote oceanic forcing, we perform the same EOF analysis for EXP_NCEP_BRY (Fig 4k-n) as seen in Fig 4a-d for EXP_NCEP. Off Peru, the first mode (EOF 1) of anomalous tracer concentration shows a similar spatial pattern between EXP_NCEP (Fig 4a) and EXP_NCEP_BRY (Fig 4k). The temporal modulation of that mode (PCs 1; Fig 4b and Fig 4l), which corresponds to an upwelling variability at the coast, is nevertheless different. When the experiment incorporates waves crossing the model boundaries (EXP_NCEP), we saw (section 3b; Fig 4b) that the first mode of upwelling variability is significantly correlated with the ENSO cycle (Fig 4b; $R=0.37$). This relationship does not appear anymore when the experiment excludes remote ocean forcing (Fig 4l; $R=0.02$). Winds drive those patterns of upwelling in both cases. But the equatorial signals modulate the strength of that upwelling by depressing or lifting the local pycnocline.

Off central Chile, the same observation can be made. The first mode of tracer concentration displays a comparable spatial pattern between the two model experiments (Fig 4c and Fig 4m) with the same decadal frequency signal in their PCs (green lines in Fig 4d and Fig 4n), described in the previous section. However, the correlation between the PCs and the Niño 3.4 index drops

from $R=0.32$ in EXP_NCEP (Fig 4d) to $R=0.14$ in EXP_NCEP_BRY (Fig 4n), confirming that this region is also very sensitive to coastally trapped Kelvin waves generating at the equator, in particular during strong El Niño events. Compared to Fig 4d (EXP_NCEP), Fig 4n (EXP_NCEP_BRY) indicates in the PC1 that, during both the 1982 and 1998 El Niño events, the strength of the anomalous downwelling is greatly reduced without the presence of those downwelling equatorial Kelvin waves.

4. Conclusion

The eastern boundary Humboldt Current System is the site of strong coastal upwelling and exceptionally high biological productivity (Ryther, 1969). In this study, the upwelling variability has been investigated using a free-surface, hydrostatic, eddy-resolving primitive equation model forced with three different sets of surface momentum fluxes (ECMWF, QSCAT and NCEP). The statistics of upwelled coastal waters were computed using a model passive tracer. Consistent with satellite observations and previous descriptions of the circulation in the HCS region, we find that the mean SSH and SST are well reproduced in EXP_QSCAT and EXP_ECMWF. The presence of the passive tracer shows the coast of Peru and central Chile as two intense (and consequently highly productive) upwelling regions. We also find that even though EXP_NCEP does not clearly capture the upwelling cells in the mean SST and shows significant differences in the mean SSH, due to a poor representation of the mean coastal NCEP winds, the non-seasonal temporal variability shows a good agreement with coastal in-situ measurements.

On the interannual time scale, much of the variability is caused by the ENSO cycle both through local changes in the surface wind stress and via

propagation of coastally trapped Kelvin waves, generated at the equator. Indeed, off Peru, an EOF analysis on the passive tracer at the surface shows that the first mode of variability is highly correlated with the Niño 3.4 index. Off central Chile the first mode also reveals a multi-decadal signal superimposed on the ENSO variability. Fig 4r indicates that this multi-decadal variability, which is also apparent in coastal station sea level observations, is consistent with local atmospheric forcing as inferred from the second mode of SLPa variability. Both EXP_NCEP and EXP_ECMWF capture a similar interannual variability.

The studies from Brink (1982), focused on the Peru region, and Leth and Middleton (2006), focused on central Chile, show that coastal trapped waves have an important contribution to the upwelling variability in those regions, which often dominate the effect of local winds, especially off Peru. The passive tracer approach used in our study also supports that view. We find that the correlation between the interannual upwelling variability and ENSO drops considerably when the model boundaries do not transmit the equatorial Kelvin waves. In particular off Peru, when the first mode of upwelling variability is strongly correlated with the Niño 3.4 index in presence of equatorial coastally trapped Kelvin waves, they become uncorrelated without. Those differences in upwelling strength are clearly seen during strong El Niño events (1982, 1997), both off Peru and central Chile.

The passive tracer experiments, performed in this study, provide a dynamical framework to interpret (and predict) how the upwelling of nutrient-rich coastal water has (and will) respond to atmospheric and oceanic forcing and therefore also allows predictions of changes in vertical and offshore advection of other important biochemical quantities. This variability could have strong

impacts in the Peru-Chile upwelling ecosystem. Earlier studies have shown that the ENSO interannual variability strongly modulates the biological productivity, species distribution and community structure in the coastal pelagic ecosystem (Ulloa et al., 2001; Escribano et al., 2004; Bertrand et al., 2008). However, the underlying mechanism associated to this variability remains poorly described. In this context, the use of ocean modeling became an important tool to understand the forces driving the fluctuations in the Humboldt ecosystem.

References

- Alheit, J. and M. Niquen, 2004: Regime shifts in the Humboldt Current ecosystem. *Progress in Oceanography* **60**(2-4): 201-222.
- Arcos, D. F., L. A. Cubillos and S. P. Nunez, 2001: The jack mackerel fishery and El Nino 1997-98 effects off Chile. *Progress in Oceanography* **49**(1-4): 597-617.
- Bertrand, S., B. Dewitte, J. Tam, E. Diaz and A. Bertrand, 2008: Impacts of Kelvin wave forcing in the Peru Humboldt Current system: Scenarios of spatial reorganizations from physics to fishers. *Progress in Oceanography* **79**(2-4): 278-289.
- Blanco, J. L., M. E. Carr, A. C. Thomas and P. T. Strub, 2002: Hydrographic conditions off northern Chile during the 1996-1998 La Nina and El Nino events. *Journal of Geophysical Research-Oceans* **107**(C3).
- Brink, K. H., 1982: A comparison of long coastal trapped wave theory with observations off Peru. *J. Phys. Oceanogr.*, **12**, 897-913.
- Combes, V., E. Di Lorenzo, et al., 2009: Interannual and Decadal Variations in Cross-Shelf Transport in the Gulf of Alaska. *Journal of Physical Oceanography* **39**(4): 1050-1059.
- Correa-Ramirez, M. A., S. Hormazabal and G. Yuras, 2007: Mesoscale eddies and high chlorophyll concentrations off central Chile (29 degrees-39 degrees S). *Geophysical Research Letters* **34**(12): 5.
- Di Lorenzo, E., A. J. Miller, N. Schneider, and J. C. McWilliams, 2005: The warming of the California current system: Dynamics and ecosystem implications. *J. Phys. Oceanogr.*, **35**, 336-362.
- Escribano, R., G. Daneri, L. Farias, V. A. Gallardo, H. E. Gonzalez, D. Gutierrez, C. B. Lange, C. E. Morales, O. Pizarro, O. Ulloa and M. Braun, 2004: Biological and chemical consequences of the 1997-1998 El Nino in the Chilean coastal upwelling system: a synthesis. *Deep-Sea Research Part II-Topical Studies in Oceanography* **51**(20-21): 2389-2411.
- Gunther, E. R., 1936. A report on oceanographical investigation in the Peru Coastal Current. *Discovery Rep.*, **13**, 107-276.
- Halpern, D., 2002: Offshore Ekman transport and Ekman pumping off Peru during the 1997-1998 El Nino. *Geophysical Research Letters* **29**(5): 4.
- Hill, A. E., B. M. Hickey, F. A. Shillington, P. T. Strub, K. H. Brink, E. D. Barton, and A. C. Thomas, 1998, Eastern Ocean boundaries, in *The Sea*, vol. 11, edited by A. R. Robinson and K. H. Brink, pp. 29- 67, John Wiley, Hoboken, N. J.
- Hormazabal, S., G. Shaffer, J. Letelier and O. Ulloa, 2001: Local and remote forcing of sea surface temperature in the coastal upwelling system off Chile. *Journal of Geophysical Research-Oceans* **106**(C8): 16657-16671.
- Hormazabal, S., G. Shaffer, and O. Pizarro, 2002: Tropical Pacific control of intraseasonal oscillations off Chile by way of oceanic and atmospheric pathways. *Geophysical Research Letters* **29**(6).
- Kalnay, E., Kanamitsu, M., Kistler, R., Collins, W., Deaven, D., Gandin, L., Iredell, M., Saha, S., White, G., Woollen, J., Zhu, Y., Chelliah, M., Ebisuzaki, W., Higgins, W., Janowiak, J., Mo, K.C., Ropelewski, C., Wang, J., Leetmaa, A., Reynolds, R., Jenne, R., Joseph, D., 1996.: The NCEP/NCAR 40-year reanalysis project. *Bulletin of the American Meteorological Society* **77**, 437-471.

- Large, W. G., J. C. McWilliams, and S. C. Doney, 1994: Oceanic vertical mixing: A review and a model with a nonlocal boundary layer parameterization. *Rev. Geophys.*, **32**, 363–403.
- Leth, O. and J. F. Middleton, 2006: A numerical study of the upwelling circulation off central Chile: Effects of remote oceanic forcing. *Journal of Geophysical Research-Oceans* **111**(C12).
- Marchesiello, P., J.C. McWilliams and A. Shchepetkin, 2003: Equilibrium structure and dynamics of the California Current System. *Journal of Physical Oceanography* **33**, 753–783.
- Masumoto, Y., and Coauthors, 2004: A fifty-year eddy-resolving simulation of the World Ocean—Preliminary outcomes of OFES (OGCM for the Earth Simulator). *J. Earth Simul.*, **1**, 31–52.
- Niiler, P. P., N. A. Maximenko, and J. C. McWilliams (2003), Dynamically balanced absolute sea level of the global ocean derived from near-surface velocity observations, *Geophys. Res. Lett.*, **30**(22), 2164, doi:10.1029/2003GL018628.
- Penven, P., C. Roy, J. R. E. Lutjeharms, A. Colin de Verdière, A. Johnson, F. Shillington, P. Fre´on, and G. Brundrit, 2001: A regional hydrodynamic model of the Southern Benguela, *S. Afr. J. Sci.*, **97**, 472– 476
- Penven, P., Echevin, V., Pasapera, J., Colas, F., Tam, J., 2005: Average circulation, seasonal cycle, and mesoscale dynamics of the Peru Current System: A modeling approach. *J. Geophys. Res., Oceans*. **110** (C10).
- Pizarro, O., G. Shaffer, B. Dewitte and M. Ramos, 2002.: Dynamics of seasonal and interannual variability of the Peru-Chile Undercurrent. *Geophysical Research Letters* **29**(12).
- Ryther, J. H., 1969: Photosynthesis and fish production in the sea. *Science*, **166**, 72–76
- Shaffer, G., O. Pizarro, L. Djurfeldt, S. Salinas and J. Rutllant, 1997: Circulation and low-frequency variability near the Chilean coast: Remotely forced fluctuations during the 1991-92 El Nino. *Journal of Physical Oceanography* **27**(2): 217-235.
- Shchepetkin, A. F. and J. C. McWilliams, 2005: The regional oceanic modeling system (ROMS): a split-explicit, free-surface, topography-following-coordinate oceanic model. *Ocean Modelling*, **9**(4): 347-404.
- Spillane, M. C., D. B. Enfield, and J. S. Allen, 1987: Intraseasonal oscillations in sea level along the west coast of the Americas. *J. Phys. Oceanogr.*, **17**, 313–325.
- Strub, P. T., J. M. Mesias, V. Montecino, J. Rutllant, and S. Salinas, Coastal ocean circulation off western South America, in *The Sea*, vol. 11, edited by A. R. Robinson and K. H. Brink, pp. 273– 313, John Wiley, New York, 1998.
- Ulloa, O., N. Escribano, S. Hormazabal, R. A. Quinones, R. R. Gonzalez and M. Ramos, 2001: Evolution and biological effects of the 1997-98 El Nino in the upwelling ecosystem off northern Chile. *Geophysical Research Letters* **28**(8): 1591-1594.
- Uppala, S.M., P. W. Kallberg, A. J. Simmons, U. Andrae, V. D. Bechtold, M. Fiorino, J. K. Gibson, J. Haseler, A. Hernandez, G. A. Kelly, X. Li, K. Onogi, S. Saarinen, N. Sokka, R. P. Allan, E. Andersson, K. Arpe, M. A. Balmaseda, A. C. M. Beljaars, L. Van De Berg, J. Bidlot, N. Bormann, S. Caires, F. Chevallier, A. Dethof, M. Dragosavac, M. Fisher, M. Fuentes, S. Hagemann, E. Holm, B. J. Hoskins, L. Isaksen, P. Janssen, R. Jenne, A. P. McNally, J. F. Mahfouf, J. J. Morcrette, N. A. Rayner, R. W. Saunders, P. Simon, A. Sterl, K. E. Trenberth, A. Untch, D. Vasiljevic, P. Viterbo and J. Woollen, 2005: The ERA-40 re-analysis. *Quarterly Journal of the Royal Meteorological Society* **131**(612): 2961-3012.

Table and Figure Caption List

Table 1: Table of experiments

Fig 1: From EXP_ECMWF, (a) Model Sea Surface Height (in meters), (b) Model Surface Tracer concentration and alongshore wind stress and (c) the logarithm of Chlorophyll-a concentration (in mg m⁻³) for January 1999. (d) shows the vertical section of temperature across the black line in (b) and the meridional current (black line (positive values) and dash line (negative values), contour interval is 0.05 ms⁻¹ from -0.3 to 0.2 ms⁻¹). (e) shows the vertical section of Passive Tracer..

Fig 2: Mean from 1999 of the (a) ECMWF/QSCAT/NCEP meridional surface wind stress, (b) Sea Surface Height (SSH) from EXP_ECMWF/EXP_QSCAT/EXP_NCEP with surface currents (black vectors). (c) Sea Surface Temperature (SST) from EXP_ECMWF/EXP_QSCAT/EXP_NCEP with surface wind stress (black vectors) and (d) Surface Passive Tracer from EXP_ECMWF/EXP_QSCAT/EXP_NCEP with alongshore wind stress. Mean satellite AVISO SSH and AVHRR-AMSR SST is also shown on (b) and (c).

Fig 3: Comparison of the coastal deseasonalized SSH for Lobos de Afuera, Callao, Arica, Antofagasta and Valparaiso between the model EXP_NCEP (a) and EXP_ECMWF (b) output (red line) and in situ tide gauge data. The ocean bathymetry is shown in color on the map.

Fig 4: EOF1 and PC1 of Passive Tracer anomaly concentration off Peru (a-b) and off central Chile (c-d) for EXP_NCEP. (e-j) same as (a-d) but for EXP_ECMWF. (k-n) same as (a-d) but for EXP_NCEP_BRY. The PCs are compared with the Niño 3.4 index (purple line). (o-r) show the first and second EOF of the NCEP sea level pressure. The PC1(red line) is compared with the AAO index (purple line)

Fig 5: (a) Difference in Passive Tracer concentration between EXP_NCEP and EXP_NCEP_BRY associated with the 1997-1998 El Niño event. (b) compares the time series of anomalous tracer concentration averaged over the white box in (a) for EXP_NCEP (blue line) and EXP_NCEP_BRY (black line) with the NCEP surface meridional wind stress (green line). (c) shows the spatial correlation coefficient between the tracer concentration time series of EXP_NCEP and EXP_NCEP_BRY. (d) same as (c) for the Sea Surface Height and Eddy Kinetic Energy for EXP_NCEP (white contours, contour interval is 20 cm²s⁻² from 40 to 140 cm²s⁻²).

	Run Length	Forcing (Fluxes)	Forcing (Wind)	Initial	Boundary
EXP_SPIN	1950 - 2005	NCEP	NCEP	From OFES	
EXP_NCEP	1950 - 2007	Corrected NCEP	NCEP	From EXP_SPIN	
EXP_QSCAT	1999 - 2007		QSCAT		
EXP_ECMWF	1958 - 2002		ECMWF		
EXP_NCEP_BRY	1950 - 2007		NCEP	From EXP_SPIN	Climatology (No Kelvin waves)

Table 1: Table of experiments

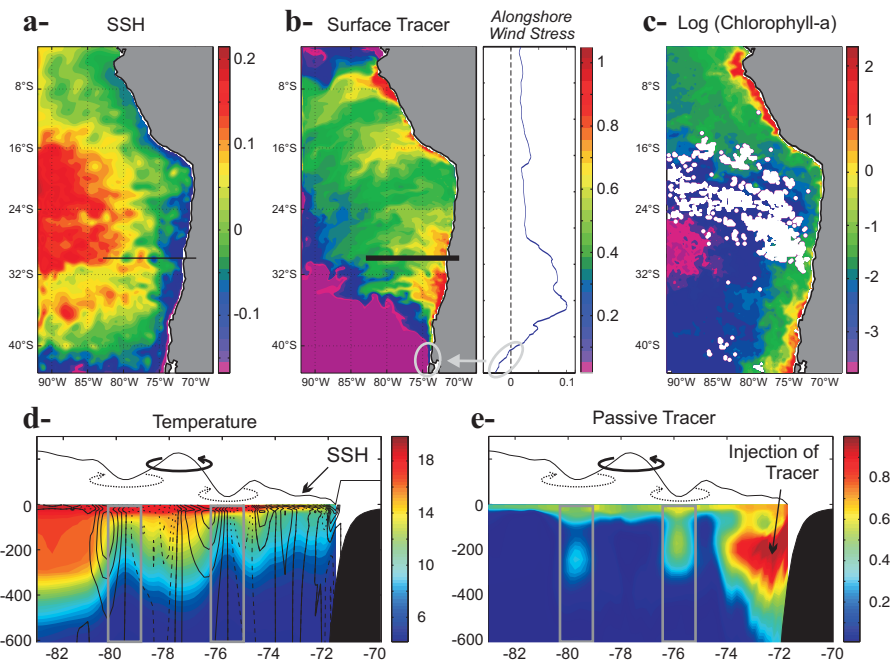
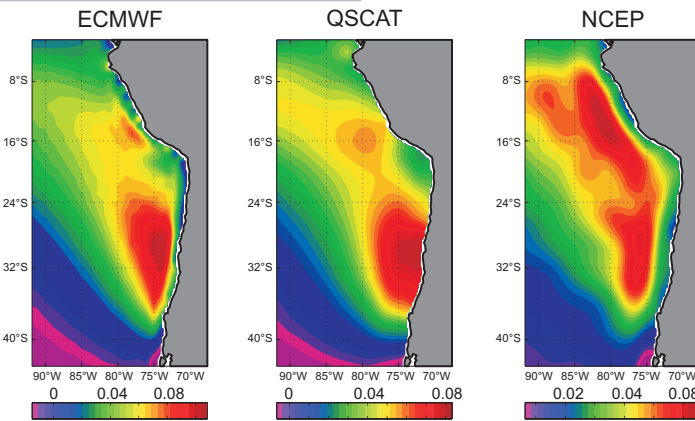
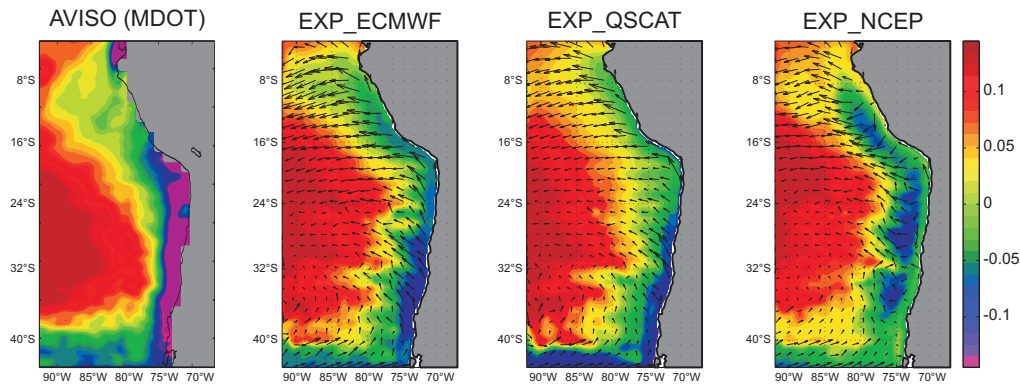


Figure 1: From EXP_ECMWF, (a) Model Sea Surface Height (in meters), (b) Model Surface Tracer concentration and alongshore wind stress and (c) the logarithm of Chlorophyll-a concentration (in mg m^{-3}) for January 1999. (d) shows the vertical section of temperature across the black line in (b) and the meridional current (black line (positive values) and dash line (negative values), contour interval is 0.05 ms^{-1} from -0.3 to 0.2 ms^{-1}). (e) shows the vertical section of Passive Tracer.

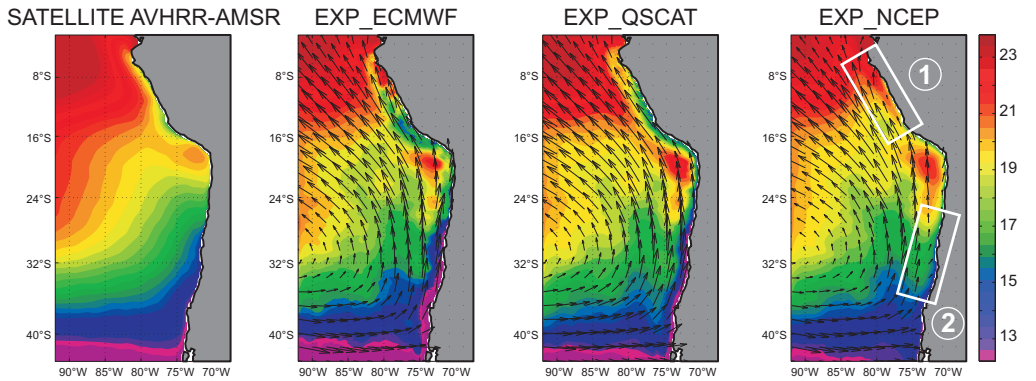
a- Meridional Surface Wind Stress



b- Sea Surface Height + Surface Currents



c- Sea Surface Temperature + Surface Wind Stress



d- Surface Tracer Concentration + Coastal Meridional Wind

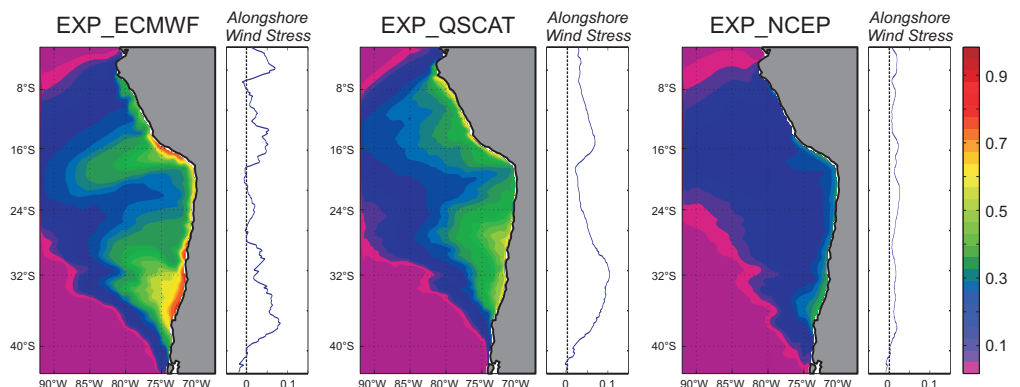


Figure 2: Mean from 1999 of the (a) ECMWF/QSCAT/NCEP meridional surface wind stress, (b) Sea Surface Height (SSH) from EXP_ECMWF/EXP_QSCAT/EXP_NCEP with surface currents (black vectors). (c) Sea Surface Temperature (SST) from EXP_ECMWF/EXP_QSCAT/EXP_NCEP with surface wind stress (black vectors) and (d) Surface Passive Tracer from EXP_ECMWF/EXP_QSCAT/EXP_NCEP with alongshore wind stress. Mean satellite AVISO SSH and AVHRR-AMSR SST is also shown on (b) and (c).

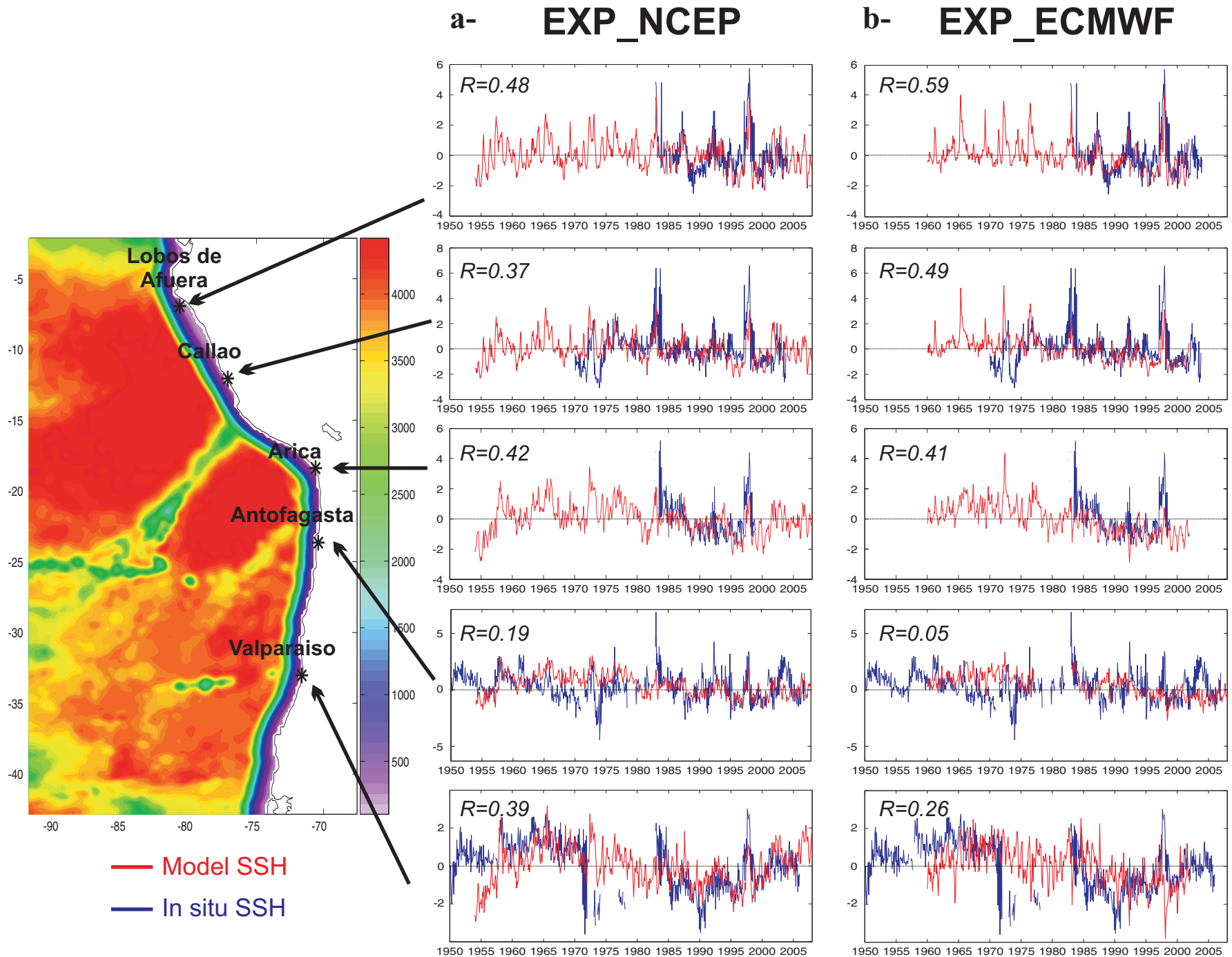
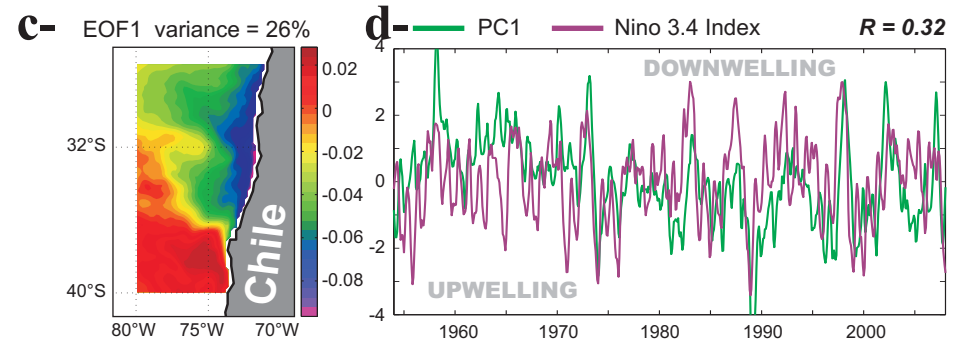
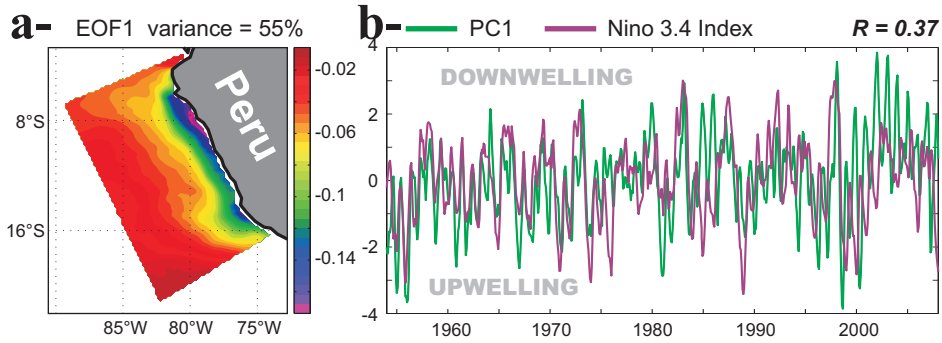
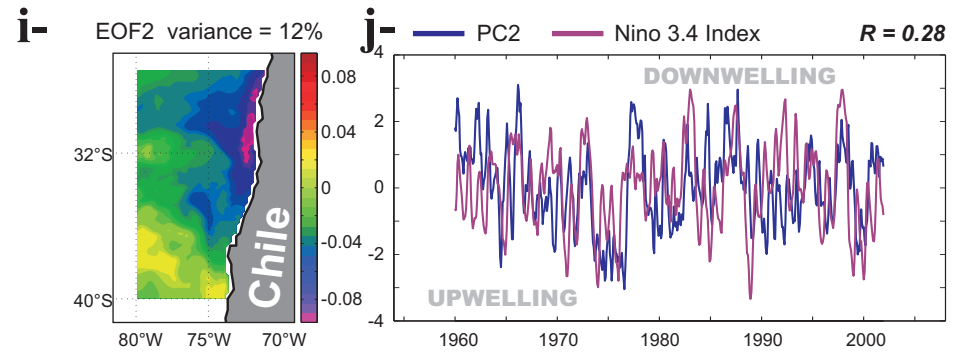
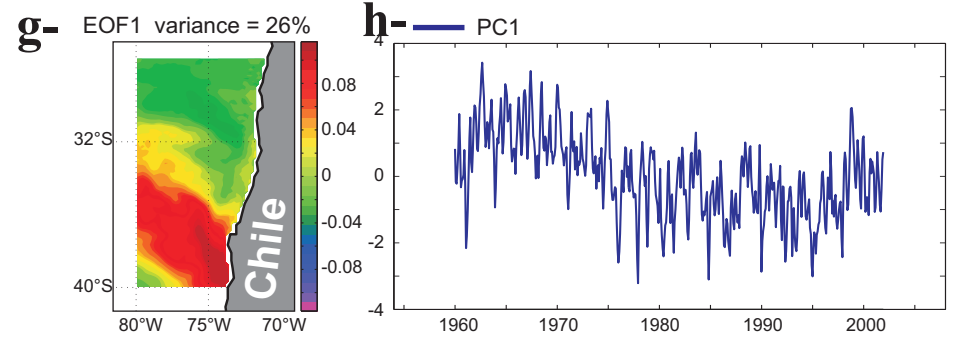
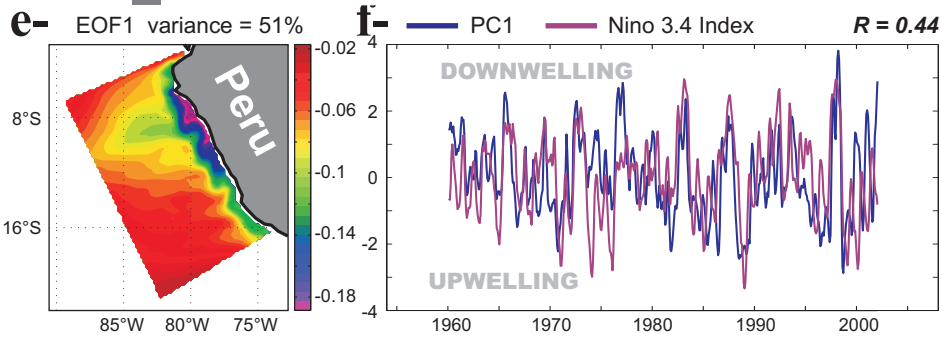


Figure 3: Comparison of the coastal deseasonalized SSH for Lobos de Afuera, Callao, Arica, Antofagasta and Valparaiso between the model EXP_NCEP (a) and EXP_ECMWF (b) output (red line) and in situ tide gauge data. The ocean bathymetry is shown in color on the map.

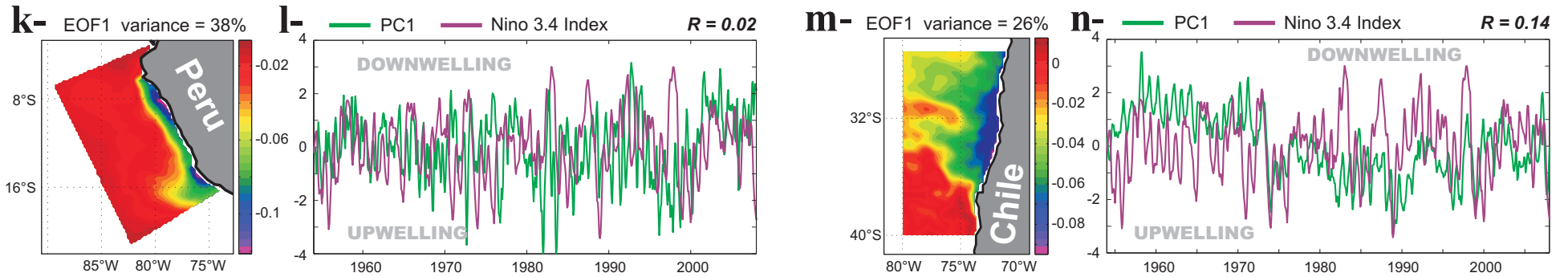
EXP_NCEP Passive Tracer



EXP_ECMWF Passive Tracer



EXP_NCEP_BRY Passive Tracer



NCEP Sea Level Pressure off central Chile

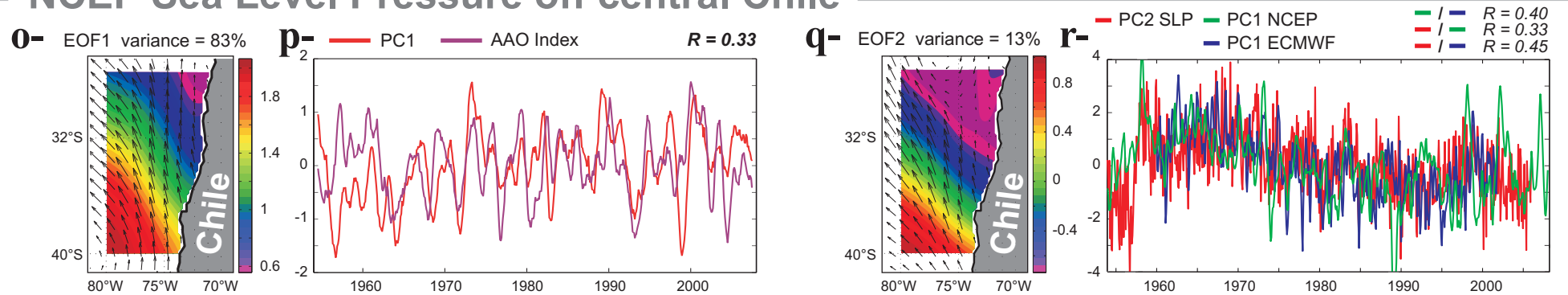
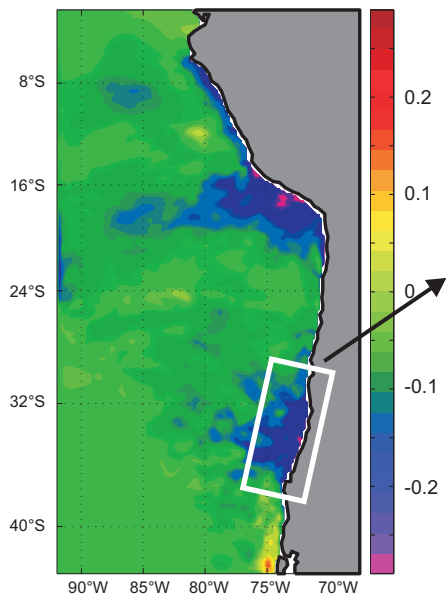
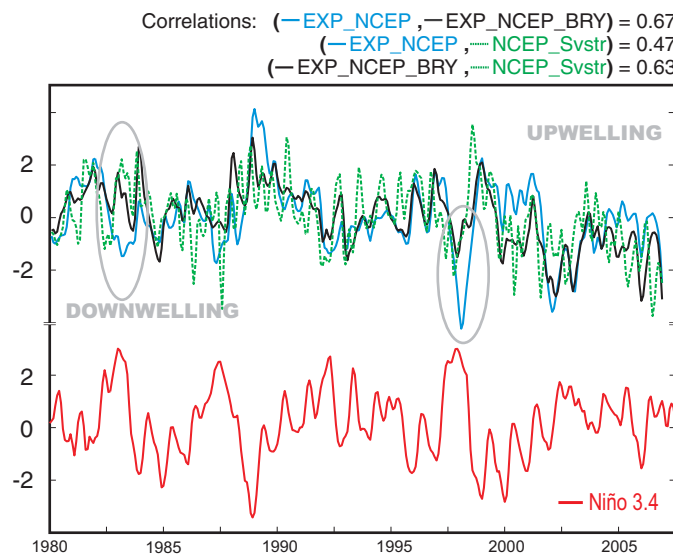


Figure 4: EOF1 and PC1 of Passive Tracer anomaly concentration off Peru (a-b) and off central Chile (c-d) for EXP_NCEP. (e-j) same as (a-d) but for EXP_ECMWF. (k-n) same as (a-d) but for EXP_NCEP_BRY. The PCs are compared with the Niño 3.4 index (purple line). (o-r) show the first and second EOF of the NCEP sea level pressure. The PC1 (red line) is compared with the AAO index (purple line)

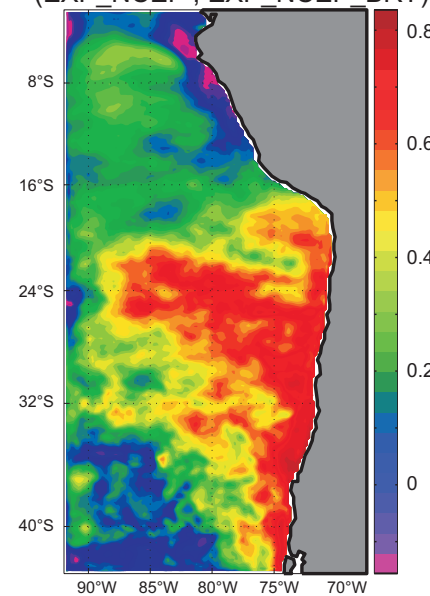
a- EXP_NCEP minus EXP_NCEP_BRY



b- anomalous tracer concentration averaged over the white box



c- Correlation Tracer (EXP_NCEP, EXP_NCEP_BRY)



d- Correlation SSH (EXP_NCEP, EXP_NCEP_BRY)

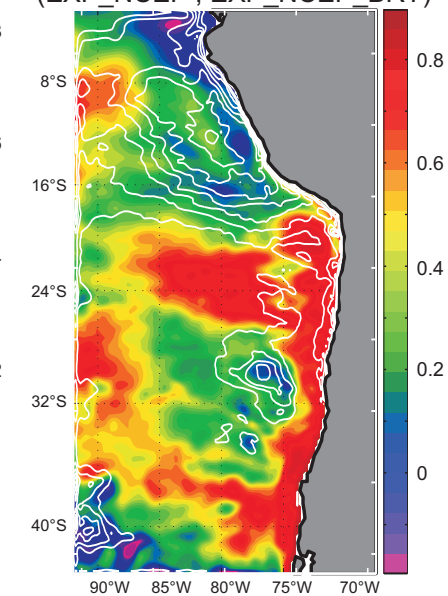


Figure 5: (a) Difference in Passive Tracer concentration between EXP_NCEP and EXP_NCEP_BRY associated with the 1997-1998 El Niño event. (b) compares the time series of anomalous tracer concentration averaged over the white box in (a) for EXP_NCEP (blue line) and EXP_NCEP_BRY (black line) with the NCEP surface meridional wind stress (green line). (c) shows the spatial correlation coefficient between the tracer concentration time series of EXP_NCEP and EXP_NCEP_BRY. (d) same as (c) for the Sea Surface Height and Eddy Kinetic Energy for EXP_NCEP (white contours, contour interval is 20 cm²s⁻² from 40 to 140 cm²s⁻²).